5. Flow Patterns of Two-Phase Systems in Microfluidic Cross-Junctions

Tetuko Kurniawan[1,3], **Mahsa Sahebdivani**[2], **Slawomir Blonski**[1], **Piotr M. Korczyk**[1]

[1] Institute of Fundamental Technological Research, Polish Academy of Sciences
Warsaw, Poland
[2] Institute of Physical Chemistry, Polish Academy of Sciences
Warsaw, Poland
[3] President University
Cikarang Baru, Bekasi, Indonesia
* Corresponding Author: piotr.korczyk@ippt.pan.pl

This study investigated two-phase flow patterns in microfluidic cross-junctions at low capillary numbers. Four distinct flow patterns were observed: at-Junction, Downstream, Parallel Flow, and Bi-modal. The occurrence of these patterns depends on the flow rate ratio and channel aspect ratio. A novel Bi-modal pattern was discovered, where two droplet formation modes appeared alternately to produce droplets of two distinct sizes, challenging the conventional understanding of uniform droplet generation. This pattern arises from the interplay between the droplet-phase thread length, its receding dynamics, and the channel geometry. These findings expand our understanding of droplet formation mechanisms in microfluidic devices and may enable novel applications in drug delivery, material synthesis, and diagnostics.
Keywords: microfluidics, cross-junction, flow-focusing device, droplet formation, two-phase flow.

https://doi.org/10.24425/9788365550682.ch5

1. Introduction

Droplet microfluidics, a specialized branch of microfluidics, has transformed biomedical applications by enabling precise high-throughput techniques for single-cell analysis [1, 2], drug delivery [3], and point-of-care diagnostics [4]. This method

leverages multiphase flow to create droplets – tiny, isolated compartments formed by immiscible fluids, typically oil and water – within microscale channels on chips. Droplets range in size from nanoliters to a few microliters and act as miniature reactors capable of isolating and encapsulating cells, molecules, or nanoparticles for controlled experiments [5]. Their small volumes reduce reagent consumption, minimize waste, and allow rapid and efficient mixing of fluids for various chemical and biochemical processes [6, 7].

Microfluidic devices can generate and manipulate thousands of droplets per second with remarkable consistency and efficiency. These droplets facilitate complex operations, such as mixing [8], merging [9], splitting [10, 11], sorting [12, 13], and trapping [14]. By combining these operations, advanced protocols such as on-demand concentration gradient generation [15] and droplet digital counting [16] can be achieved, significantly expanding the scope of droplet microfluidics applications.

At the heart of a droplet microfluidic device is a droplet generator that produces a micro-sized volume of liquid in a non-immiscible liquid. The most common type of droplet generator is a passive-type, in which droplets are generated based on the interaction between two (or more) immiscible fluids flowing through a junction of two or more channels. In the area of single-cell analysis, for example, microfluidic junctions such as co-flow, T-junction, and flow-focusing are commonly used to produce monodisperse droplets with sizes ranging from a few tens to hundreds of microns for high-throughput cell culture experiments [17].

A thorough mechanistic understanding of droplet formation is essential for the effective use of microfluidic junctions in various applications. In particular, droplet volume control requires careful consideration of flow conditions, channel geometry, and fluid properties. Because the dimensions of microchannels typically range from a few tens to a few hundreds of micrometers, conventional body forces, such as gravity and inertia, have only a minor effect on the flow. Instead, fluid behavior at this scale is dominated by the interplay between viscous and interfacial forces. To capture this balance, the capillary number (Ca) is commonly used, representing the ratio of viscous forces to interfacial forces.

In multiphase systems involving two immiscible fluids, variations in the capillary number alone can give rise to at least ten distinct flow patterns [18]. The range of possible patterns expands further when additional factors are introduced, such as the geometry of the microfluidic junction [19] and wetting properties of the liquid–surface interface [20]. These considerations highlight the inherent complexity of multiphase flow in microfluidic channels and underscore the importance of understanding the physical mechanisms governing droplet generation.

For flow patterns that produce droplets, it is widely accepted that fixed flow inputs generate monodisperse droplets – droplets with uniform size. This phenomenon has numerous applications, the most common of which is as a tool for single-cell analysis [21]. However, our research demonstrates that by subtly mod-

ifying the hydrodynamic junction geometry, it is possible to produce two or more distinct droplet sizes using fixed flow inputs, without incorporating additional active control elements.

In this unique flow pattern, two different droplet formation modes alternate, resulting in the production of two (or more) consistent droplet sizes. We have termed this pattern 'Bi-modal' owing to its characteristic dual-size output. This study aims to provide a comprehensive description and analysis of this novel flow pattern, exploring its mechanisms, potential applications, and implications for microfluidic technology.

The discovery of the Bi-modal pattern challenges the conventional understanding of droplet generation in microfluidic systems and opens up new possibilities for precise control over the droplet size distribution. That is, two or more droplet size distributions can be produced precisely without any additional control elements for the flow input, whereas previously, only a single droplet size distribution could be produced from such a system.

2. Materials and methods

2.1. Experimental setup

Five microfluidic cross-junction devices were fabricated in-house for the purpose of this study. The chip is made of two polycarbonate (PC) plates (Macrolon). Channels were engraved on both plates using the CNC milling machine (Ergwind MFG 4025P), which has a resolution of 5 µm. The two plates were bonded together using a hot press at 135 °C for 12 min. There was no modification to the surface of the microfluidic channel. Each device has rectangular cross-section channels with a constant aspect ratio, as shown in Table 1.

Table 1. Dimensions of the five chips prepared for the study of the droplet formation. W and H are the width and height of the channel, respectively. The device aspect ratio, W/H, is defined as the ratio between the width and height of the channel.

Width W [µm]	Height H [µm]	Aspect ratio W/H [–]
2010	494	4.07
1510	495	3.05
955	469	2.04
752	525	1.43
501	525	0.95

As illustrated in Fig. 1, the continuous phase (CP) and droplet phase (DP) liquids were delivered using separate computer-controlled syringe pumps (Cetoni Nemesys) loaded with 1 mL glass syringes (ILS 2624016) or 500 µL glass syringes (Hamilton 81220). Each syringe pump controlled the flow rate of the

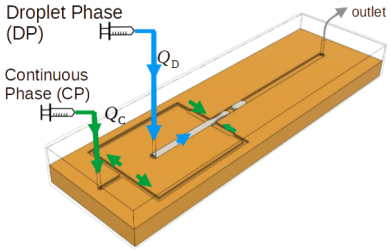

Fig. 1. Schematic of the experimental setup for droplet formation in a cross-junction device.

CP and DP, which are denoted as Q_C and Q_D, respectively (see Fig. 1). The CP and DP fluids were hexadecane 95 % (Sigma Aldrich) and fluorinated oil FC-40 (3M), respectively. The fluid pairs were chosen to ensure the wetting condition of the PC surface channel with CP without the need for a surfactant. Thus, the effect of the surfactant was excluded. The interfacial tension between the CP and DP, γ, is 7.3 N/m, which was measured using the pendant drop method at 21 °C. The viscosities of hexadecane and fluorinated oil are $\mu_C = 3.6\,\mathrm{mPa}\cdot\mathrm{s}$ and $\mu_D = 4.1\,\mathrm{mPa}\cdot\mathrm{s}$, respectively, as measured using a falling-ball viscometer at 21 °C. Initially, testing was performed at the lowest flow rates to ensure that no flow fluctuations were caused by the mechanical components of the pump within the range of parameters investigated in this study [22]. The syringes were connected to the inlets of the devices using polyethylene (Beckton-Dickinson PE-60) or polytetrafluoroethylene (Bola S1810-10) tubing. The same tubing was used to connect the outlet of the chip to the waste container.

2.2. Image acquisition

A stereo microscope (Zeiss Stemi 508) equipped with a CCD camera (IDS UI-3274LE-C-HQ) was used to observe the droplet formation. In the high temporal and spatial resolution experiments intended to observe the formation process at the junction, the recording frame rate was set to 45 fps. For experiments to measure droplet length and observe various flow patterns, a frame rate between 1 and 20 fps was used, depending on the flow rate of the DP. In a device with a high aspect ratio and a very low flow rate, the period between droplet pinch-off can be longer than 30 min, or in other words, approximately one hour per droplet. Thus, low frame rate recording reduces the video file size and does not affect the measurements in these experiments.

2.3. Image processing

The recorded images were analyzed using a script written in the Python 3 programming language, utilizing various packages supporting image analysis [23, 24]. The typical droplet image analysis procedure (algorithm) is as follows:

1. An RGB image was flattened into a grayscale image, as shown in Fig. 2a.
2. If a background image containing an empty junction is available, the interface of a forming droplet can be easily extracted by subtracting the intensity of the droplet-containing image from the background image, as shown in Fig. 2b.
3. If the background image is not available, it can be produced using another image processing technique. In the case of a bright-field image with uniform light coming from the back of the chip, a background image can be created by taking the maximum intensity from many images with different droplet positions. Because the interface of a droplet is a shadow (low-intensity value), the interface is replaced with higher-intensity pixels from other images.

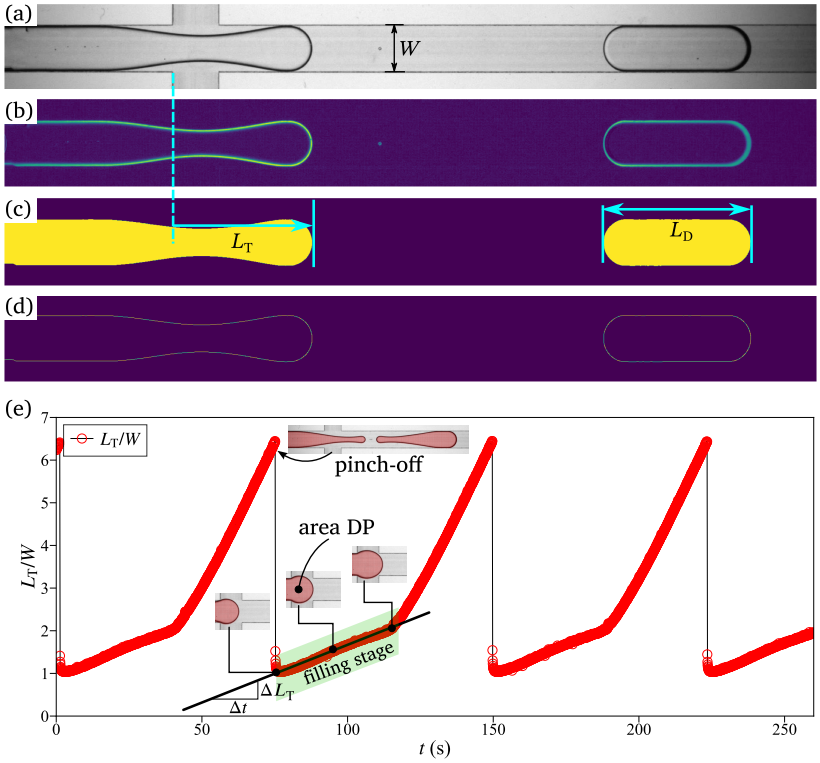

Fig. 2. Example of image processing result: (a) original grayscale image, (b) image containing the droplet shadow only as a result of subtraction with the background image, (c) image containing a filled droplet (these images were useful for measuring the droplet area), (d) image containing an outline of the droplets is useful for measuring the parameters obtained from the interface, (e) measurement result of L_T versus time. A jump in L_T marks the pinch-off of the droplet formation. In the filling stage, the droplet flows into the junction at the rate of the DP flow rate, Q_D. Thus, the increase in the droplet area is equal to Q_D/H, as illustrated in the three images with the shaded areas. Images were sourced from [25].

4. The grayscale droplet image was then converted into a binary image by applying a threshold value.
5. Image noise was reduced by executing one or a combination of morphological operations, such as erosion, dilation, opening, closing, and removal of small objects.
6. After noise removal, the resulting image contained only a droplet outline (Fig. 2d), and various parameters were measured. If required, the area enclosed by the outline can be filled by replacing the zero values within the outline with a binary value of 1, as shown in Fig. 2c.

The exact implementation of the algorithms varies depending on the quality of the recorded images. An example of the resulting measurement of the droplet tip position, L_T, is shown as red circles in Fig. 2e.

A jump in the L_T value indicates a pinch-off. Following the pinch-off, the DP recedes into the cross-junction and starts to grow at a rate proportional to the filling rate of the DP, that is, $\frac{dL_T}{dt} \propto \frac{Q_D}{HW}$. More accurately, the filling rate of the DP can be approximated by measuring the area within the growing droplet over time (see images with a red overlay). The rate of change in the droplet area is approximately equal to Q_D/H. This method can be used to verify the DP flow rate, Q_D.

3. Results and discussion

3.1. Flow patterns at low Ca regime

Multiple flow patterns can arise when two immiscible fluids flow through microfluidic junctions. The emergence of these patterns depends on the channel geometry, relative magnitudes of the two liquid flow rates, and physical properties of the fluids, such as viscosity and interfacial tension.

Consider a cross-junction device (see Figs. 1 or 2), where the droplet phase (DP) enters with a flow rate of Q_D and encounters the continuous phase (CP) with a flow rate of Q_C. The flow at this length scale and within a confined space is dominated by viscous and interfacial forces, which are captured by the Capillary number,

$$\mathrm{Ca} = \frac{\mu_C Q_C}{\gamma W H}, \tag{1}$$

where μ_C is the viscosity of the CP, γ is the interfacial tension, and W and H are the channel width and height, respectively.

The behavior of droplet formation strongly depends on Ca [18]. At higher Ca, the viscous drag from the CP is sufficient to deform the DP without requiring the DP to occupy the junction. Droplet breakup then occurs via the dripping or jetting mechanism, producing droplets smaller than the channel width [19]. In con-

trast, at low Ca, the droplet formation occurs only after the DP grows large enough to obstruct the outlet channel. This obstruction causes the CP to accumulate, squeezing the DP and eventually breaking it into a droplet larger than the channel width. This mechanism is known as *squeezing* droplet formation, and it depends on the junction geometry [26]. Bi-modal droplet generation is also geometrically dependent and has been found in this low Ca regime. Therefore, the present study focuses exclusively on the low Ca regime. Since only a single fluid pair is used in this study, μ_C and γ are constants. Thus, Ca depends on the device aspect ratio (see Table 1) and the CP flow rate, Q_C. In this study, the operating CP flow rate ranges from 0.01 mL/h to 14 mL/h, covering Ca values between 7×10^{-6} and 5×10^{-3} across different devices.

Within this Ca regime, a variety of flow patterns emerge as a function of the ratio between two flow rates:

$$q = \frac{Q_D}{Q_C}. \tag{2}$$

These results are summarized in flow pattern maps (see Fig. 3), where the key control parameter is the flow rate ratio in combination with the channel aspect ratio, W/H. Four distinct flow patterns were observed:

1. **at-Junction**: For small q, the CP pinches off the DP near the junction, causing the DP thread to recede into the inlet channel (see blue regions in Figs. 3a–f).
2. **Downstream**: At an intermediate q, droplet pinch-off occurs further downstream. After pinch-off, the receding DP thread remained inside the outlet channel, leading to a different breakup mechanism (see orange regions in Figs. 3a–f).
3. **Parallel Flow**: For a higher q, the CP flow was insufficient to deform and break the DP. Instead, the two phases flow side by side, forming a stable filament (see green regions in Fig. 3a–f).
4. **Bi-modal**: In a narrow range of q, both at-Junction and Downstream modes appear alternatingly, producing droplets of two distinct sizes. This occurs primarily in channels with the cross-sectional aspect ratio, W/H, equal to or larger than two, as indicated by the yellow-cross markers in Figs. 3d–f.

As shown in Figs. 3b–f, the flow pattern map is unique for each device aspect ratio. This implies that the transitional flow rate ratio depends on the device W/H. The transitional flow rate ratio between Parallel Flow and Downstream is denoted as $q_{P\to D}$, while the transitional flow rate ratio between Downstream (including Bi-modal) and at-Junction is denoted $q_{D\to J}$. As shown in Figs. 3g and 3h, both $q_{P\to D}$ and $q_{D\to J}$ decrease with increasing device aspect ratio. We observed that the inverse of $q_{P\to D}$ was linearly proportional to the device aspect ratio, which is in agreement with the previous report by Humphry *et al.* [27].

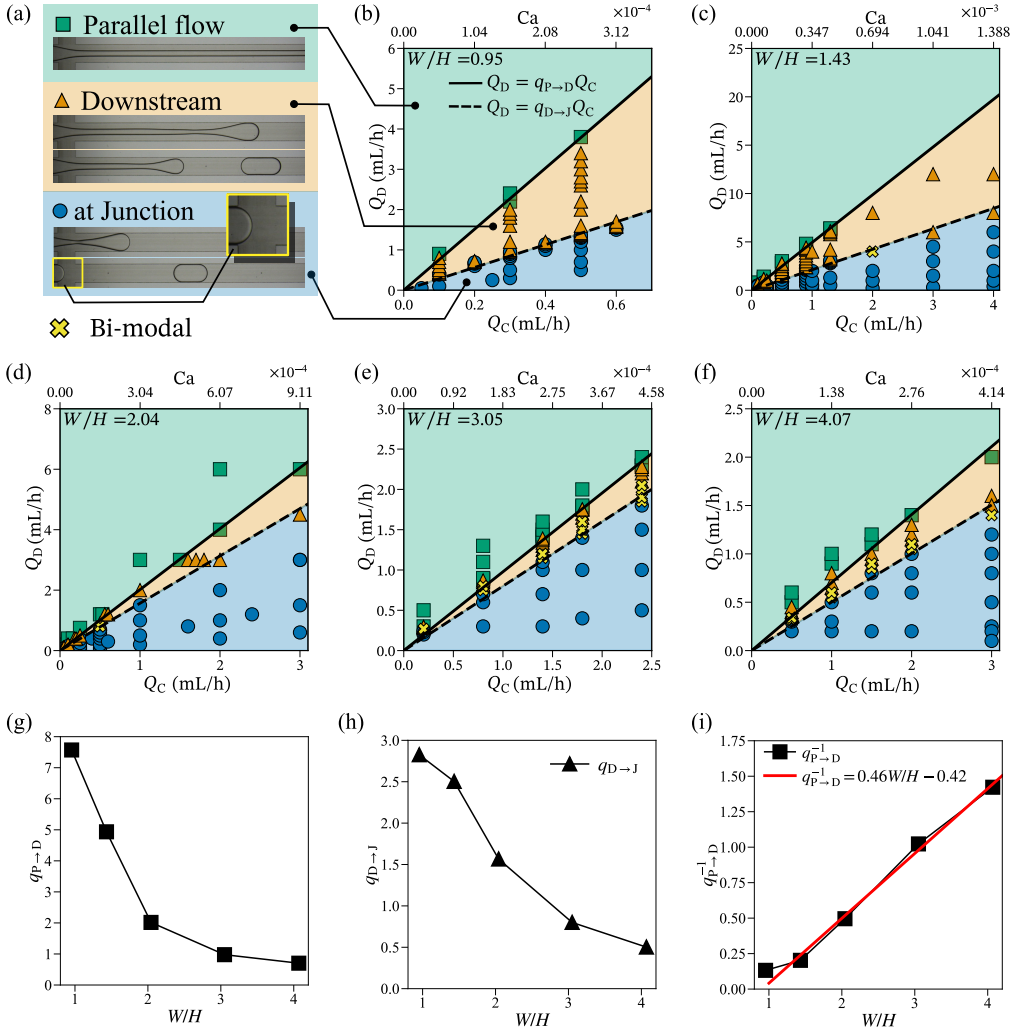

Fig. 3. Observation of flow patterns in the low-Ca flow regime: (a) flow pattern emerging owing to different flow-rate ratios, (b)–(f) flow pattern maps for different device aspect ratios, (g) $q_{P\to D}$ and (h) $q_{D\to J}$ decrease with increasing device aspect ratio W/H, (i) Linear proportionality of the inverse of $q_{P\to D}$ against W/H. Images (a)–(f) were adapted and images (g)–(i) were reproduced from [28].

3.2. Droplet formation – at-Junction

Three-dimensional images illustrating the droplet formation process in the cross-junction device with W/H of one and four are shown in Figs. 4a and 4b, respectively. The experimental images of at-Junction droplet formation are shown in Fig. 4c. From the image sequence, parameters such as the droplet tip length L_T and the local maxima and minima of droplet E were measured and plotted over

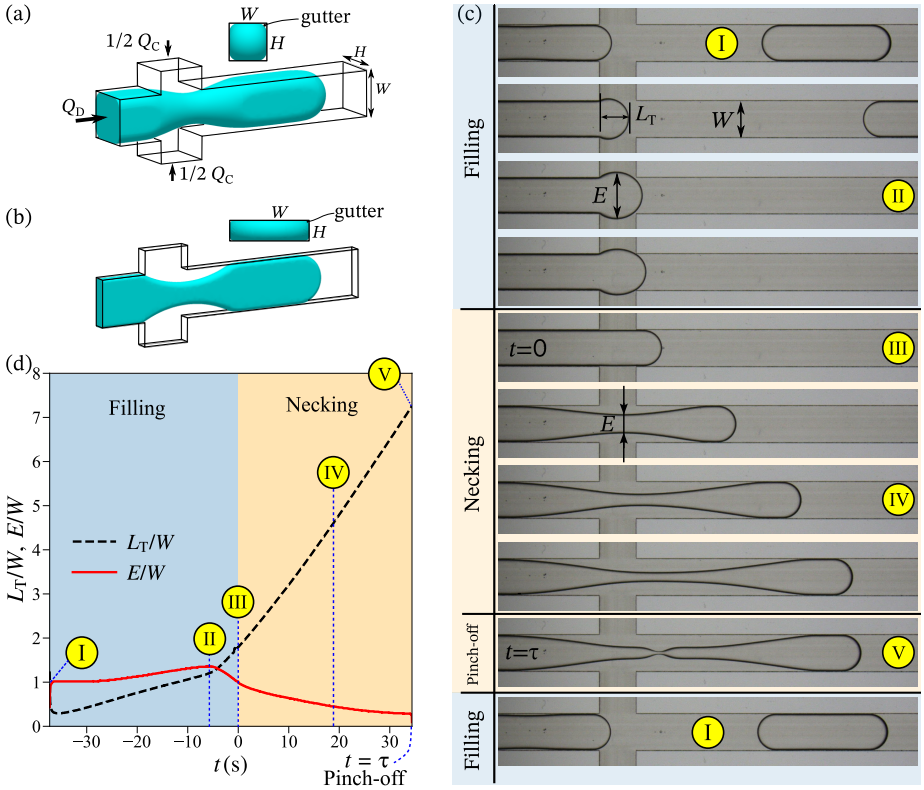

Fig. 4. Three-dimensional illustration of droplet formation in a cross-junction with W/H: (a) 1 and (b) 4. (c) Evolution of the droplet tip L_T and local maxima/minima of the forming droplet, E, in a single droplet formation cycle. (d) at-Junction droplet formation stages: filling, necking, and pinch-off. The filling stage ends when the DP blocks the outlet channel and attains a straight droplet shape, $E \approx W$. The necking time is taken from the end of the filling stage $t = 0$ s up to pinch-off $t = \tau$. Experimental images and measurements were obtained from the device with $W/H = 4.07$ at $Q_C = 1.00$ mL/h and $Q_D = 0.30$ mL/h. Images (a), (b), and (d) were reproduced, and image (c) was adapted from [28].

time, t (Fig. 4d). As shown in the image sequence, at-Junction droplet formation consists of three stages:

– **Filling.** This is the stage when the DP flows through the junction and has not yet occupied the outlet channel. The CP flows through the junction and directly to the outlet channel with minimal interference from the DP. Eventually, the DP becomes sufficiently long to fill the junction and outlet channels. The end of the filling stage is marked when the droplet becomes a straight plug, $E \approx W$, as shown by the II markings in Figs. 4c and 4d.

– **Necking**. Time zero of the necking stage is taken when the DP forms a straight plug, as shown by the III markings in Figs. 4c and 4d. As the

DP occupies the outlet channel and blocks the path for the CP, it increases the flow resistance for the CP flow passing through the droplet. Consequently, the CP accumulated upstream of the droplet tip and began to squeeze the DP. This process is called necking (see IV in Figs. 4c and 4d). The necking process ends when the neck of the droplet becomes thin enough to become unstable owing to the Plateau–Rayleigh instability.

– **Pinch-off**. The instability drives the collapse of the thin neck, producing a droplet of DP (see V in Figs. 4c and 4d). This process occurs in a very short time and is called the pinch-off.

3.3. Droplet formation – Downstream

The Downstream droplet formation process is similar to the at-Junction mode, except that because of the higher flow rate ratio, necking occurs much further downstream of the junction, as shown in Fig. 5a. After pinch-off, the

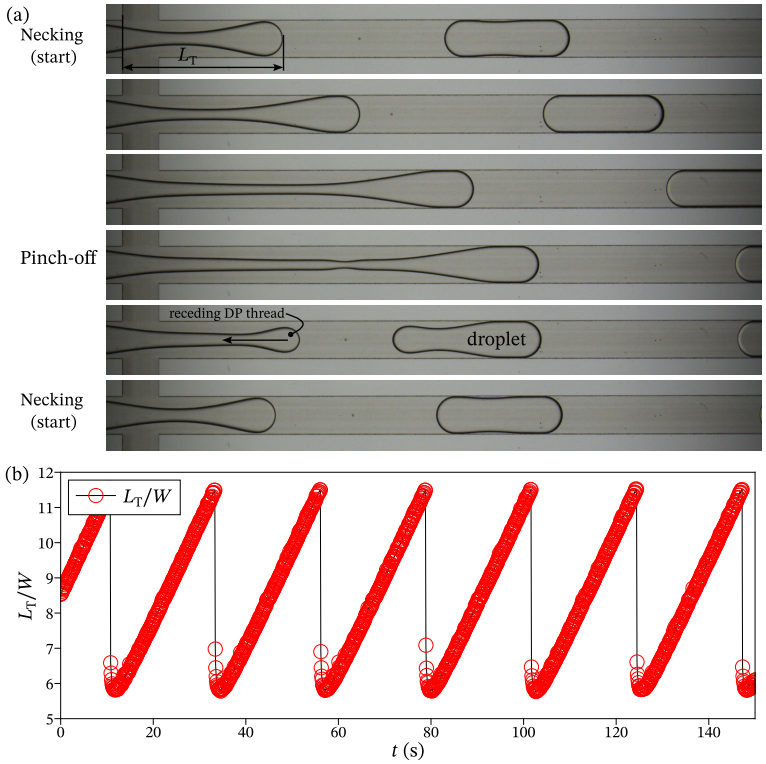

Fig. 5. (a) Downstream droplet formation occurs in two stages: necking and pinch-off. (b) Droplet tip length cycle shows that the process begins with the relaxation of the DP thread, continues with the necking phase, and concludes with the pinch-off. Experimental images and measurements were obtained from the device with $W/H = 4.07$ under flow conditions of $Q_C = 1.50\,\mathrm{mL/h}$ and $Q_D = 0.90\,\mathrm{mL/h}$. Images were sourced from [25].

droplet thread (i.e., the droplet phase that is part of the DP supply line) recedes and stops inside the outlet channel. The process is then followed by the necking stage, skipping the filling stage. Thus, the Downstream droplet formation consisted of only two stages: necking and pinch-off, as shown in Fig. 5a. The measurement of L_T in this mode (see Fig. 5b) also shows that after the jump (pinch-off), L_T evolves almost linearly with time until it jumps again. This is in contrast to the evolution of L_T in the at-Junction mode (Fig. 4d), where there are two different regions of L_T evolution.

3.4. Bi-modal droplet formation

Bi-modal droplet formation consists of two formation modes: at-Junction and Downstream. The two modes appeared alternately, as shown in the image sequence in Fig. 6. The image sequence with green (dark) and brown (light) backgrounds shows the at-Junction and Downstream modes, respectively. Initially, the droplet undergoes the normal at-Junction droplet formation process: filling, necking, and finally pinch-off. However, because the thread is sufficiently long, the receding thread after pinch-off remains inside the outlet channel. Next,

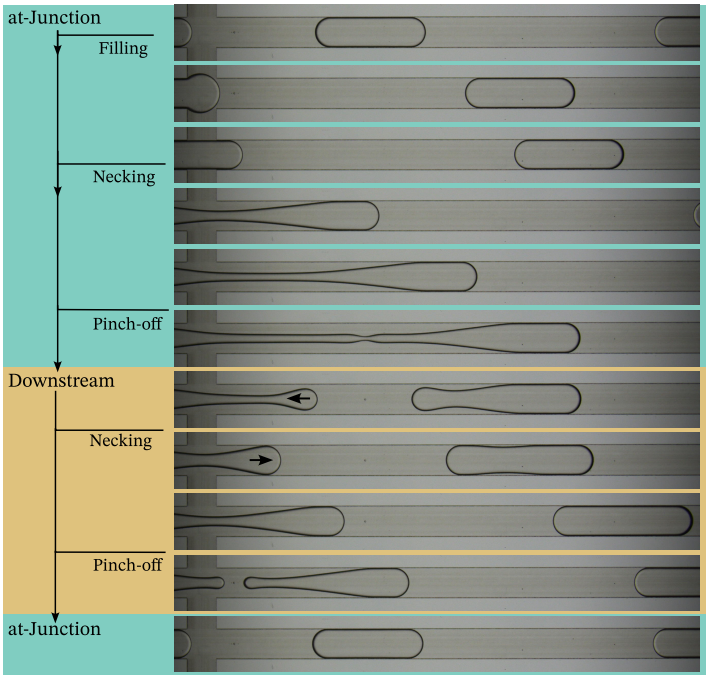

Fig. 6. Image sequence of one full cycle of bi-modal droplet formation. At-Junction (green) is followed by Downstream (brown), and then followed again by at-Junction (green). Images were captured from the device with $W/H = 4.07$ at $Q_C = 0.50\,\mathrm{mL/h}$ and $Q_D = 0.20\,\mathrm{mL/h}$. Images were sourced from [25].

the thread grows inside the channel while undergoing necking until pinch-off. The key to the process that allows the alternating condition between two modes is that there must be a sufficient length of droplet thread during at-Junction droplet formation, such that the receding thread after the pinch-off stops inside the outlet channel, allowing subsequent droplet formation in the Downstream mode. However, the droplet thread (resulting from the at-Junction mode) cannot be too long; otherwise, only cycles of the Downstream droplet formation can occur.

The two modes produced two distinct droplet sizes. The droplet size produced in the at-Junction mode was larger than that produced in the Downstream mode. This is because the overall droplet formation duration is shorter in the Downstream mode, as shown by the measurement of L_T in Fig. 7a. The evolution of L_T clearly indicates the alternating modes, with the green and brown regions appearing alternately, showing the at-Junction and Downstream modes, respectively. The at-Junction mode takes a longer time – shown by the wider green

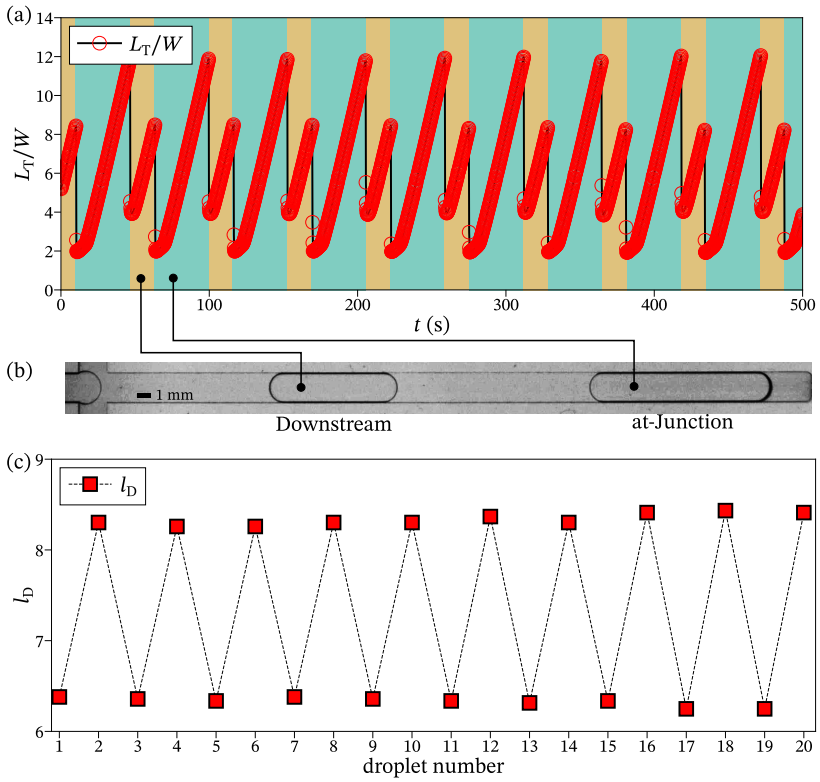

Fig. 7. (a) Evolution of L_T shows two modes of droplet formation: at-Junction (green) and Downstream (brown). (b) Experimental image showing two distinct droplet sizes. (c) Sequential pattern of two different droplet sizes. Measurements were taken from the device with $W/H = 4.07$ at $Q_C = 1.50\,\mathrm{mL/h}$ and $Q_D = 0.85\,\mathrm{mL/h}$. Images were sourced from [25].

area in Fig. 7a – because each cycle consists of filling and necking stages. Because the time for droplet formation was longer, the size of the droplet produced by the at-Junction mode was larger (see Fig. 7b). The Downstream mode only has cycles of the shorter necking stage, producing a smaller droplet size. The measurement shown in Fig. 7c shows the sequential alternating of two droplet sizes.

4. Conclusions

This study provides a comprehensive analysis of two-phase flow patterns in microfluidic cross-junction devices, focusing on the low capillary number regime. Four distinct flow patterns were identified: at-Junction, Downstream, Parallel Flow, and Bi-modal. The transitions between these patterns were found to depend on both the flow rate ratio and channel aspect ratio. Of particular interest is the novel Bi-modal pattern, which produces alternating droplet sizes under fixed flow conditions. This pattern challenges the conventional understanding of droplet generation in microfluidic systems and opens up new possibilities for precise control over the droplet size distribution.

This study provides detailed insights into the mechanisms of droplet formation for the at- Junction, Downstream, and Bi-modal patterns. The at-Junction mode consists of three stages (filling, necking, and pinch-off), whereas the Downstream mode involves only necking and pinch-off. The Bi-modal pattern alternates between these two modes, resulting in the production of two distinct droplet sizes. This unique behavior is attributed to the specific conditions that allow the dispersed-phase thread to recede and stop within the outlet channel after pinch-off.

These findings may have significant implications for various applications of droplet microfluidics, including single-cell analysis, drug delivery, and advanced diagnostics. The discovery of the Bi-modal pattern, in particular, offers new opportunities for generating controlled distributions of droplet sizes without the need for additional active control elements. This breakthrough could potentially revolutionize fields that rely on droplet-based technologies, enabling sophisticated and precise manipulation of microscale fluid dynamics.

Acknowledgements

Tetuko Kurniawan acknowledges the support within the Preludium 23 grant (UMO-2024/53/ N/ST8/04010) from the National Science Centre, Poland. Paperpal and Claude Sonnet 4 were used to provide grammatical corrections and to generate suggestions for polishing the language.

References

1. Jammes F.C., Maerkl S.J., How single-cell immunology is benefiting from microfluidic technologies, *Microsystems and Nanoengineering*, **6**(1): 45, 2020.
2. Li B. *et al.*, Droplets microfluidics platform–A tool for single cell research, *Frontiers in Bioengineering and Biotechnology*, **11**: 1121870, 2023.
3. Kung C.-T. *et al.*, Microfluidic synthesis control technology and its application in drug delivery, bioimaging, biosensing, environmental analysis and cell analysis, *Chemical Engineering Journal*, **399**: 125748, 2020.
4. Mu H.-Y. *et al.*, Microfluidic-based approaches for COVID-19 diagnosis, *Biomicrofluidics*, **14**(6): 061504, 2020.
5. Yuan H. *et al.*, Microfluidic screening and genomic mutation identification for enhancing cellulase production in Pichia pastoris, *Biotechnology for Biofuels and Bioproducts*, **15**(1): 50, 2022.
6. Song H., Chen D.L., Ismagilov R.F., Reactions in droplets in microfluidic channels, *Angewandte Chemie International Edition*, **45**(44): 7336–7356, 2006.
7. Kaminski T.S., Garstecki P., Controlled droplet microfluidic systems for multistep chemical and biological assays, *Chemical Society Reviews*, **46**(20): 6210–6226, 2017.
8. Gu S.-Q. *et al.*, Multifunctional picoliter droplet manipulation platform and its application in single cell analysis, *Analytical Chemistry*, **83**(19): 7570–7576, 2011.
9. Bremond N., Thiam A.R., Bibette J., Decompressing emulsion droplets favors coalescence, *Physical Review Letters*, **100**(2): 024501, 2008.
10. Link D.R. *et al.*, Geometrically mediated breakup of drops in microfluidic devices, *Physical Review Letters*, **92**(5): 054503, 2004.
11. Chen Y. *et al.*, Three-dimensional splitting microfluidics, *Lab on a Chip*, **16**(8): 1332–1339, 2016.
12. Mazutis L., Griffiths A.D., Preparation of monodisperse emulsions by hydrodynamic size fractionation, *Applied Physics Letters*, **95**(20): 204103, 2009.
13. Hatch A.C. *et al.*, Passive droplet sorting using viscoelastic flow focusing, *Lab on a Chip*, **13**(7): 1308–1315, 2013.
14. Huebner A. *et al.*, Static microdroplet arrays: A microfluidic device for droplet trapping, incubation and release for enzymatic and cell-based assays, *Lab on a Chip*, **9**(5): 692–698, 2009.
15. Zaremba D., Blonski S., Korczyk P.M., Concentration on demand – A microfluidic system for precise adjustment of the content of single droplets, *Chemical Engineering Journal*, **430**: 132935, 2022.
16. Zaremba D., Blonski S., Korczyk P.M., Integration of capillary–hydrodynamic logic circuitries for built-in control over multiple droplets in microfluidic networks, *Lab on a Chip*, **21**(9): 1771–1778, 2021.

17. Sart S. *et al.*, Cell culture in microfluidic droplets, *Chemical Reviews*, **122**(7): 7061–7096, 2022.

18. Yao C. *et al.*, Two-phase flow and mass transfer in microchannels: A review from local mechanism to global models, *Chemical Engineering Science*, **229**: 116017, 2021.

19. Lee W., Walker L.M., Anna S.L., Role of geometry and fluid properties in droplet and thread formation processes in planar flow focusing, *Physics of Fluids*, **21**(3): 032103, 2009.

20. Cubaud T., Mason T.G., Capillary threads and viscous droplets in square microchannels, *Physics of Fluids*, **20**(5): 053302, 2008.

21. Joensson H.N., Andersson Svahn H., Droplet microfluidics—A tool for single-cell analysis, *Angewandte Chemie International Edition*, **51**(49): 12176–12192, 2012.

22. Korczyk P.M. *et al.*, Accounting for corner flow unifies the understanding of droplet formation in microfluidic channels, *Nature Communications*, **10**(1): 2528, 2019.

23. van der Walt S. *et al.*, scikit-image: image processing in Python, *PeerJ*, **2**: e453, 2014.

24. Harris C.R. *et al.*, Array programming with NumPy, *Nature*, **585**(7825): 357–362, 2020.

25. Kurniawan T., *Droplet Generation in Microfluidic Cross-Junctions: Mechanisms and Applications as Cell Incubators*, PhD Thesis, Institute of Fundamental Technological Research, Polish Academy of Sciences, 2025.

26. Garstecki P. *et al.*, Formation of droplets and bubbles in a microfluidic T-junction—scaling and mechanism of break-up, *Lab on a Chip*, **6**(3): 437–446, 2006.

27. Humphry K.J. *et al.*, Suppression of instabilities in multiphase flow by geometric confinement, *Physical Review E*, **79**(5): 056310, 2009.

28. Kurniawan T. *et al.*, Formation of droplets in microfluidic cross-junctions at small capillary numbers: Breakdown of the classical squeezing regime, *Chemical Engineering Journal*, **474**: 145601, 2023.